N-Alkyl substituted 1*H*-benzimidazoles as improved n-type dopants for a naphthalene-diimide based copolymer†

B. Saglio,[ab] M. Mura,[a] M. Massetti,[bc] F. Scuratti,[bd] D. Beretta, [b] X. Jiao,[e] C. R. McNeill, [e] M. Sommer, [f] A. Famulari,[a] G. Lanzani, [bc] M. Caironi*[b] and C. Bertarelli*[ab]

Doped polymer semiconductors are actively studied for opto- and micro-electronic applications including thermoelectric generators, where a high electrical conductivity is a key factor. In general, n-type doping is more challenging to achieve than p-type doping. Here we study n-type doping of a commonly used electron transporting naphthalene-diimide bithiophene copolymer with a series of air-stable and solution-processable benzimidazole dopants. To understand the role of dopant structure on miscibility and the resulting conductivity, benzimidazoles with different linear and branched alkyl substituents were synthesized, and their doping efficacy compared through combined morphological, electrical and thermoelectric characterization. We observe a clear dependence of the nature of the alkyl substituent on dopant intercalation into the semicrystalline morphology. By increasing the length or the steric hindrance of the alkyl substituents, the miscibility between dopant and copolymer is enhanced leading to optimized electrical conductivity.

Introduction

Conjugated polymers have found application in various electronic devices, including transistors and circuits,[1–4] solar cells[5] and light emitting diodes.[6,7] Charge transport in polymer films is largely governed by the polymer chemical structure and solid-state packing of interacting conjugated segments.[8] Research in this field has led to a rationalization of the molecular design and a better understanding of the charge transport mechanism. Through the establishment of structure–property relationships,[9–11] tailored structures and optimized processing have led to enhanced electronic performance.

For most electronic and opto-electronic devices, it is desirable to tune the electrical conductivity (σ) through doping in order to enable optimized devices. More recently, the increased interest in polymer thermoelectrics[12,13] as cost-effective waste heat energy converters has re-activated research in molecular doping to achieve high and controllable values of σ. Doping of conjugated polymers is typically achieved by the addition of molecular dopants that produce an increase in the number of free charge carriers and hence of σ.

p-Type conducting polymers and related dopants have been deeply investigated in past years and impressive conductivity values have been recently achieved.[14–16] On the contrary, for the case of the n-type counterparts, which are required to enable thermocouples for efficient thermoelectric generators, examples are still limited. Issues limiting n-type conducting polymers are related to ambient stability: while stable electron transporting materials are known, their corresponding radical anions that form upon doping are prone to undergo re-oxidation to the neutral form if exposed to *e.g.* humidity or oxygen.[17] The extent of the instability of the radical anion to ambient conditions strongly depends on the position of the lowest unoccupied molecular orbital (LUMO) level, as demonstrated for example in rylene diimides.[18] n-Type dopants strongly suffer from air-instability, as well.

n-Type doping of polyacetylene was first performed under inert atmosphere using metal complexes, such as sodium and potassium naphthalene,[19] with elemental dopants such as Na, K, Li and Cs,[20–23] or alternatively, inorganic salts as Li_2CO_3, Na_2CO_3, K_2CO_3, Cs_2CO_3, and $LiNH_2$ (ref. 24–28) have also been proposed. However, such doping could only be carried out by evaporation at high temperatures, which is less attractive than solution-based techniques; moreover, inorganic ions often affect the device
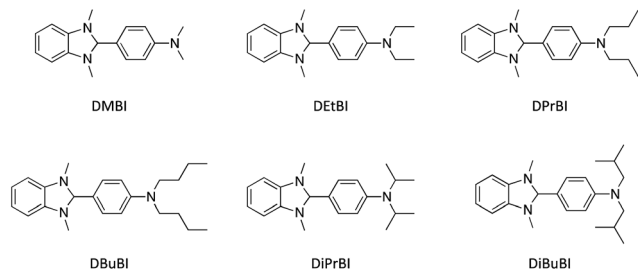
Fig. 1 Molecular structure of N-alkyl substituted 1H-benzimidazoles.

operation lifetime since they diffuse through the organic layer. Aromatic donor compounds, e.g. TTF[29,30] or BEDT–TTF,[31] form charge transfer complexes and can be processed from solution, while being unstable in air. This last issue can be overcome by stable precursors, which can be in situ converted into the dopant upon thermal or light activation, e.g. 1H-benzimidazole derivatives such as **DMBI**–POH[32] or the organic salt o-MeO-**DMBI**-I.[33] The latter can only be processed by evaporation.

In 2010, Bao et al. first reported n-type dopant 1,3-dimethyl-2-2-phenyl-2,3-dihydro-1H-benzoimidazole (**DMBI**) – which had been previously reported as a reagent for the reduction of organic compounds[34] – as an effective, solution processable and air-stable dopant to significantly increase the conductivity of phenyl-C_{61}-butyric acid methyl ester (PCBM).[35] Later, Schlitz et al.[36] used the same compound to dope poly(N,N'-bis-2-octyldodecylnaphthalene-1,4,5,8-bis-dicarboximide-2,6-diyl-alt-5,5'-2,2'-bithiophene) P(NDI2OD-T2), obtaining an increase of the electrical conductivity of about five orders of magnitude, reaching 5 × 10^{-4} S cm^{-1}. In the same study a poor miscibility of the dopant and P(NDI2OD-T2) was reported, i.e. phase segregation occurred at high dopant concentration, limiting the effectiveness of the doping and the maximum conductivity that could be achieved. Another limitation relates to the strong charge localization in the polymer, as evidenced by Fabiano et al.[37]

Here we address the miscibility issue by studying the effect of the benzimidazole alkyl substituents on the doping efficiency. With electronic effects of the alkyl substituents on electron transfer being negligible, we have designed and synthesized a series of 1H benzimidazoles in which the N-alkyl substituents have been systematically varied (Fig. 1). This strategy is aimed at increasing dopant solubility and miscibility with P(NDI2OD-T2) through an enhanced interaction with its alkyl side chains.

In contrast to recent work that has focused on dopant/copolymer miscibility by controlling backbone curvature[38] or varying chain length or chain branching,[39,40] we show here that a tailored modification of the dopant structure towards longer and bulkier alkyl substituents has a strong effect on miscibility and doping efficiency.

Experimental

Dopant synthesis

Unless otherwise stated, all chemicals and solvents were purchased from Sigma Aldrich and used as received. Reactions of air- and water-sensitive reagents and intermediates were carried out in dried glassware under argon. Thin layer chromatography was performed by using silica gel on aluminum foil. NMR spectra were acquired on a Bruker ARX400. Mass spectroscopy was carried out with a Bruker Esquire 3000 plus.

4-Bromo-N,N-dipropylaniline (2d). N,N-Dipropylaniline (1 g, 5.64 mmol, 1 eq.) was dissolved in 17 ml dry DMF, and the solution was stirred at −18 °C under argon. NBS (1.05 g, 5.92 mmol, 1.05 eq.), dissolved in 5 ml dry DMF, was dropwise added over a period of 1.5 hours. Then the reaction mixture was stirred at −18 °C for 3.5 hours and at room temperature overnight. The reaction mixture was separated between dichloromethane (DCM)/water, the water phase extracted with DCM, the DCM layers combined, dried over Na_2SO_4 and concentrated under reduced pressure. A suspension of the residue in Et_2O was filtered, and the filtrate was washed with 3 M NaOH aqueous solution and water, dried over Na_2SO_4, and concentrated under reduced pressure. The crude product was purified by flash chromatography with silica gel and hexane : ethyl acetate (9 : 1) to give the product as an orange oil in 83% yield.

^{1}H NMR (d6-benzene, 400 MHz): ppm 7.29 (dt, J = 9.17 Hz, J = 3.42 Hz, J = 2.26 Hz, 2H H–Ph), 6.27 (dt, J = 9.17 Hz, J = 3.42 Hz, J = 2.26, 2H, H–Ph), 2.79 (t, J = 7.58, 4H, N–CH_2), 1.29 (m, J = 7.58, J = 7.40, 4H, –CH_2–), 0.65 (t, J = 7.40, 6H, CH_3).

4-Bromo-N,N-diisopropylaniline (2e). N,N-Diisopropylaniline (546 mg, 3.08 mmol, 1 eq.) was dissolved in 3 ml anhydrous acetonitrile under argon. NBS (548 mg, 3.08 mmol, 1 eq.), dissolved in 3 ml anhydrous acetonitrile, was added dropwise at 0 °C over 30 minutes. The reaction mixture was stirred at 0 °C for 1 hour and then at room temperature overnight. Water was added, the reaction mixture was extracted with hexane, the organic phase dried over Na_2SO_4 and the solvent removed under reduced pressure. The crude product was purified by flash chromatography with hexane : ethyl acetate (8 : 2) as eluent, obtaining the pure product as an orange oil with 48% yield. ^{1}H NMR (d$_6$-benzene, 400 MHz): ppm 7.25 (dt, J = 9.17 Hz, J = 3.42 Hz, J = 2.26, 2H H–Ph), 6.52 (dt, J = 9.17 Hz, J = 3.42 Hz, J = 2.26 Hz, 2H, H–Ph), 3.33 (sestet, J = 6.72 Hz, 2H, N–CH), 0.89 (d, J = 6.72 Hz, 12H, –CH_3).

4-Bromo-N,N-diisobutylaniline (2f). The reaction was carried out according to the procedure of **2e**. The crude product was purified by flash chromatography using hexane : chloroform 9 : 1 as eluent to give **2f** as an orange oil in 21% yield. ^{1}H NMR (d$_6$-benzene, 400 MHz): ppm 7.28 (m, J = 9.17 Hz, J = 3.42 Hz, J = 2.26, 2H H–Ph), 6.32 (m, J = 9.17 Hz, J = 3.42 Hz, J = 2.26, 2H, H–Ph), 2.79 (d, J = 7.34 Hz, 4H, N–CH_2), 1.84 (m, J = 6.72 Hz, 2H, –CH), 0.68 (d, J = 6.72 Hz, 12H, –CH_3).

4-(Dipropylamino)benzaldehyde (3d). Compound **2d** (1.20 g, 4.68 mmol, 1 eq.) was dissolved in 9 ml anhydrous THF and the solution was cooled to −78 °C under an argon atmosphere. 2.5 M n-BuLi (in n-hexane, 4.77 mmol, 1.02 eq.) was added dropwise and the reaction mixture was stirred for 30 minutes at the same temperature. Anhydrous DMF (9.4 ml) was added and the solution was kept stirring at −78 °C for 30 minutes. Then the mixture was warmed up to room temperature, quenched with 70 ml of water and extracted with DCM (3×). The combined organic layers were dried with Na_2SO_4. After solvent removal, the crude product was purified by flash

chromatography with hexane : ethylacetate (8 : 2) to give a yellow oil in 54% yield. ^{1}H NMR (d$_6$-benzene, 400 MHz): ppm 9.85 (s, 1H, *CHO*) 7.70 (d, *J* = 8.92 Hz 2H *H*–Ph), 6.35 (d, *J* = 8.92 Hz, 2H, *H*–Ph), 2.77 (t,*J* = 7.64 Hz, 4H, N–*CH₂*), 1.24 (m,*J* = 7.46 Hz,*J* = 7.70 Hz, 4H, *CH₂*–CH₃), 0.60 (t,*J* = 7.40 Hz 6H, CH₂–*CH₃*).

4-(Diisopropylamino)benzaldehyde (3e). The reaction was carried out according to the procedure of **3d**. ^{1}H NMR (d$_6$-benzene, 400 MHz): ppm 9.60 (s, 1H, *CHO*) 7.56 (d, *J* = 8.07 Hz, 2H *H*–Ph), 6.73 (d, *J* = 8.07 Hz, 2H, *H*–Ph), 3.89 (m,*J* = 6.48,*J* = 6.66 Hz,*J* = 6.91 Hz 2H, N–*CH*), 1.23 (d,*J* = 6.72 Hz, 12H, CH₂–*CH₃*) (yield: 50%).

4-(Isobutyl(isopropyl)amino)benzaldehyde (3f). The reaction was carried out according to the procedure of **3d**. ^{1}H NMR (d$_6$-benzene, 400 MHz): ppm 9.60 (s, 1H, *CHO*) 7.59 (d, *J* = 8.92 Hz 2H *H*–Ph), 6.59 (d, *J* = 8.92 Hz, 2H, *H*–Ph), 3.14 (d, *J* = 7.34 Hz, 4H, N–*CH₂*), 2.00 (m,*J* = 6.85 Hz,*J* = 6.78 Hz, 2H, CH₂–*CH*), 0.81 (d,*J* = 6.60 Hz, 12H, CH–*CH₃*) (yield: 67%).

4-(1,3-Dimethyl-2,3-dihydro-1*H*-benzo[*d*]imidazol-2-yl)-*N,N*-dimethylaniline (DMBI). The synthetic procedure of this compound was previously reported by Naab.[41] *N,N*′-Dimethyl-*o*-phenylenediamine (1.00 mmol, 1 eq.), *N,N*′-dimethyl-1,2-phenylenediamine (1.00 mmol, 1 eq.) and a drop of glacial acetic acid were dissolved in 2 ml of methanol. The mixture was sonicated for 5 hours, followed by storage in the fridge overnight. The precipitate was filtered and washed with methanol to obtain **DMBI** as white powder in 26% yield. ^{1}H NMR (d6-DMSO, 400 MHz): ppm 7.33 (d, *J* = 8.74 Hz, 2H, H–Ph), 5.25 (d, *J* = 8.74 Hz, 2H, H–Ph), 6.58 (m,*J* = 3.18 Hz,*J* = 2.01 Hz, 2H, H–Ph), 6.39 (m,*J* = 3.18,*J* = 2.20 Hz, 2H, H–Ph), 4.73 (s, 1H, N–H–N), 2.93 (s, 6H, N–CH₃), 2.44 (s, 6H, N–CH₃).

4-(1,3-Dimethyl-2,3-dihydro-1*H*-benzo[*d*]imidazol-2-yl)-*N,N*-diethylaniline (DEtBI). The reaction was carried out according to the procedure of **DMBI**. ^{1}H NMR (d$_6$-DMSO, 400 MHz): ppm 7.29 (d,*J* = 8.74 Hz, 2H, *H*–Ph), 6.69 (d, *J* = 8.74 Hz, 2H, *H*–Ph), 6.58 (m, *J* = 3.18 Hz, *J* = 2.01 Hz, 2H, *H*–Ph), 6.39 (m, *J* = 3.18 Hz, *J* = 2.01 Hz, 2H, *H*–Ph), 4.71 (s, 1H, N–*H*–N), 3.35 (m,*J* = 7.27 Hz,*J* = 7.95 Hz, 4H, N–*CH₂*), 2.45 (s, 6H, N–*CH₃*), 1.11 (t,*J* = 6.85 Hz, 6H, CH₂–*CH₃*) (yield: 42%).

4-(1,3-Dimethyl-2,3-dihydro-1*H*-benzo[*d*]imidazol-2-yl)-*N,N*-dipropylaniline (DPrBI). The reaction was carried out according to the procedure of **DMBI**. ^{1}H NMR (d$_6$-DMSO, 400 MHz): ppm 7.27 (d, *J* = 8.74 Hz, 2H, *H*–Ph), 6.65 (d, *J* = 8.74 Hz, 2H, *H*–Ph), 6.58 (m, *J* = 3.18 Hz, *J* = 2.01 Hz, 2H, *H*–Ph), 6.39 (m, *J* = 3.18 Hz, *J* = 2.01 Hz, 2H, *H*–Ph), 4.67 (s, 1H, N–*H*–N), 3.24 (m,*J* = 7.46 Hz,*J* = 7.58, 4H, N–*CH₂*), 2.44 (s, 6H, N–*CH₃*), 1.54 (m,*J* = 7.58 Hz, 4H, CH₂–*CH₂*–CH₃), 0.89 (m,*J* = 9.00 Hz,*J* = 7.40 Hz, 6H, CH₂–*CH₃*) (yield: 17%).

***N,N*-Dibutyl-4-(1,3-dimethyl-2,3-dihydro-1*H*-benzo[*d*]imidazol-2-yl)aniline (DBuBI).** The reaction was carried out according to the procedure of **DMBI**. ^{1}H NMR (d$_6$-DMSO, 400 MHz): ppm 7.28 (d,*J* = 8.74 Hz, 2H, *H*–Ph) 6.66 (d, *J* = 8.74 Hz, 2H, *H*–Ph), 6.58 (m, 3.18 Hz,*J* = 2.01 Hz, 2H, *H*–Ph), 6.39 (m,*J* = 3.18 Hz,*J* = 2.01 Hz, 2H, *H*–Ph), 4.70 (s, 1H, N–*H*–N), 3.27 (q,*J* = 7.24 Hz, 4H, N–*CH₂*), 2.45 (s, 6H, N–*CH₃*), 1.52 (m,*J* = 8.07 Hz,*J* = 6.91 Hz, 4H, CH₂–*CH₂*–CH₂), 1.34 (m,*J* = 7.58 Hz,*J* = 7.35 Hz,

4H, CH₂–CH₂–*CH₂*), 0.93 (t, *J* = 7.34 Hz, 6H, CH₂–*CH₃*) (yield: 31%).

4-(1,3-Dimethyl-2,3-dihydro-1*H*-benzo[*d*]imidazol-2-yl)-*N,N*-diisopropylaniline (DiPrBI). The reaction was carried out according to the procedure of **DMBI**. ^{1}H NMR (d$_6$-DMSO, 400 MHz): ppm 7.27 (d,*J* = 8.74 Hz, 2H, *H*–Ph), 6.84 (d,*J* = 8.74 Hz, 2H, *H*–Ph), 6.59 (m,*J* = 3.18 Hz,*J* = 2.01 Hz, 2H, *H*–Ph), 6.40 (m, *J* = 3.18 Hz, *J* = 2.01 Hz, 2H, *H*–Ph), 4.69 (s, 1H, N–*H*–N), 3.84 (m,*J* = 6.78 Hz,*J* = 6.85, 2H, N–*CH*), 2.45 (s, 6H, N–*CH₃*), 1.21 (d, *J* = 6.85 Hz, 12H, CH–*CH₃*) (yield: 31%).

4-(1,3-Dimethyl-2,3-dihydro-1*H*-benzo[*d*]imidazol-2-yl)-*N,N*-diisobutylaniline (DiBuBI). The reaction was carried out according to the procedure of **DMBI**. ^{1}H NMR (d$_6$-DMSO, 400 MHz): ppm 7.26 (d,*J* = 8.74 Hz, 2H, *H*–Ph), 6.67 (d,*J* = 8.74 Hz, 2H, *H*–Ph), 6.58 (m,*J* = 3.18 Hz,*J* = 2.01 Hz, 2H, *H*–Ph), 6.39 (m, *J* = 3.18 Hz,*J* = 2.01 Hz, 2H, *H*–Ph), 4.67 (s, 1H, N–*H*–N), 3.16 (d, *J* = 7.09 Hz, 4H, N–*CH₂*), 2.44 (s, 6H, N–*CH₃*), 1.99 (m, *J* = 6.72 Hz,*J* = 6.97 Hz, 2H, N–CH₂–*CH*) 0.87 (d,*J* = 6.60 Hz, 12H, CH–*CH₃*) (yield: 55%).

Sample preparation and doping procedure. The samples were prepared starting from a solution of P(NDI2OD-T2) (Polyera ActivInk N2200, M_n = 29 kDa, purchased from Flexterra Inc.), in 1,2-dichlorobenzene (DCB) that was heated to 80 °C and stirred for 1 hour. The concentration of the solutions used for films for variable temperature electrical conductivity, room temperature conductivity and Seebeck coefficient measurements were 5 mg ml^{-1}, 10 mg ml^{-1} and 20 mg ml^{-1}, respectively. The solution was filtered with a 0.45 μm pore size polytetrafluoroethylene (PTFE) filter. The dopant was dissolved in DCB at a concentration of 10 mg ml^{-1}. Aliquots of dopant were added to 100 μl of the pristine polymer solution and mixed at room temperature. Dopant concentrations between 10% to 50% were tested. Except for Seebeck coefficient measurements (see below), films were spin coated in an N$_2$ glovebox at 1000 rpm for 90 s and then at 3000 rpm for 10 s onto glass substrates, previously cleaned with acetone and iso-propanol and treated with an oxygen plasma for 10 minutes. Films were annealed on a hot plate at ≈150 °C for six hours in N$_2$ glovebox.

Electrical conductivity measurements. Two 50 nm thick gold contacts were evaporated (MB-ProVap-3) on the films leading to devices with an inter-electrode distance of 7 mm and width of 12 mm. Prior to measurement, samples were annealed at ≈80 °C for 10 minutes under N$_2$. Measurements were taken under N$_2$ atmosphere and at ambient temperature with a 2-point method with a Keysight Technologies semiconductor parameter analyzer (SPA).

Seebeck coefficient measurements. The polymer/dopant solutions were deposited by spin coating (1000 rpm for 60 s) onto 2 cm × 1 cm glass substrates and then annealed at 120 °C for 30 minutes in a nitrogen glovebox. The Seebeck measurements were carried out in vacuum at 90 °C, after an overnight annealing treatment at 130 °C in order to avoid any thermal effect during the measurement, using the system described in Beretta *et al.*[42]

Temperature-dependent electrical conductivity measurements. Four 50 nm thick gold contacts were evaporated on the films leading to devices with an inter-electrodes distance of

3 mm and width of 5 mm. Prior to four-point conductivity measurement, samples were annealed at $\approx 150\ ^{\circ}$C overnight in vacuum. The four-point probes measurements were taken in vacuum in the temperature range between 200 K and 300 K, with a ΔT of 10 K between each step. Downward and upward scans were performed in order to check the absence of hysteresis during the measurements.

Atomic force microscopy. Sample preparation was identical as for the electrical characterization. Topographies were measured with Agilent 5500 atomic force microscope working in acoustic mode. All images are presented with the same colour scale.

Grazing incidence wide angle X-ray scattering. GIWAXS measurements were performed at the SAXS/WAXS beamline at the Australian Synchrotron.[43] 11 keV photons were used with scattering patterns recorded on a Dectris Pilatus 1 M detector. Images shown were acquired at an incident angle close to the critical angle. Such images were chosen from a series of images taken with incident X-ray angle varying from 0.05° to 0.25° in steps of 0.01° with the chosen image showing the highest scattering intensity. The X-ray exposure time was 3 s such that no film damage was identified. The sample-to-detector distance was calibrated using a silver behenate sample. The results were analyzed by an altered version of the NIKA 2D[44] based in IgorPro.

Differential scanning calorimetry. Pristine dopants were measured on a Perkin-Elmer DSC 8500 instrument equipped with a liquid nitrogen cooling system (Perkin-Elmer CLN2) under N_2 at 10 K min^{-1}. Blend samples were prepared from o-DCB solution, thoroughly dried and placed into the heating pans. Measurements were acquired on a NETZSCH DSC 204 F1 Phoenix® under N_2 at 10 K min^{-1}.

Thermogravimetry. TGA was performed on a Perkin Elmer TGA 4000 between 50–650 °C under N_2 at 10 K min^{-1}.

Results and discussion

The six dopant molecules synthesised are shown in Fig. 1. **DMBI** has been studied before and features methyl substituents. 4-(1,3-Dimethyl-2,3-dihydro-1H-benzo[d]imidazol-2-yl)-N,N-diethylaniline (**DEtBI**) has ethyl substituents, 4-(1,3-dimethyl-2,3-dihydro-1H-benzo[d]imidazol-2-yl)-N,N-dipropylaniline (**DPrBI**) has n-propyl substituents and N,N-dibutyl-4-(1,3-dimethyl-2,3-dihydro-1H-benzo[d]imidazol-2-yl)aniline (**DBuBI**) has n-butyl substituents. **DMBI**, **DEtBI**, **DMPrBI** and **DBuBI** thus have linear chains of increasing length. In contrast, 4-(1,3-dimethyl-2,3-dihydro-1H-benzo[d]imidazol-2-yl)-N,N-diisopropylaniline (**DPrBI**) and 4-(1,3-dimethyl-2,3-dihydro-1H-benzo[d]imidazol-2-yl)-N,N-diisobutylaniline (**DiBuBI**) have branched alkyl substituents of different size. The general synthetic scheme consists of the ultrasound-assisted coupling between the N,N'-dimethyl-1,2-benzendiamine and the N-alkyl substituted p-aminobenzaldehyde (Fig. 2). For the synthesis of **DMBI**, **DEtBI** and **DBuBI** the procedure previously reported for **DMBI**[41] was followed, starting from the commercially available N,N-dialkyl aminobenzaldehydes. The products were precipitated in the reaction mixture at low temperature, separated by filtration and washed with small portions of methanol. For the synthesis of the other dopants (**DPrBI**, **DiPrBI**, **DiBuBI**), the starting compound was the N,N-dialkyl substituted aniline, which was first brominated in p-position with N-bromosuccinimide (NBS), lithiated with n-butyllithium and quenched with DMF affording the N,N-dialkylaminobenzaldehyde (Fig. 2). The resulting compound was finally coupled with N,N'-dimethyl-1,2-phenylenediamine and products (**2d–f**) were precipitated and separated by filtration. We have also tried to synthesize 1H-benzimidazoles with longer alkyl chains (i.e. hexyl), but we could not isolate the pure product by precipitation according to the procedure described for all the other compounds.

The temperature stability and phase transitions of the dopants were investigated using thermogravimetry (TGA) and differential scanning calorimetry (DSC). From TGA, onset temperatures for degradation under N_2 of ~ 200 °C can be extracted (Fig. SI 1†). Melting points T_m between 60 °C and 120 °C were observed for all dopants, with longer alkyl substituents leading to lower T_m values (Fig. SI 2–7†).

As a general procedure to test the n-doping ability of these new N-alkyl substituted 1H-benzimidazoles, aliquots of each dopant dissolved in anhydrous DCB were separately added to P(NDI2OD-T2) solutions with a dopant concentration varying from 10 to 50 wt%. The room temperature conductivity of thin films spin-coated as a function of dopant concentration is shown in Fig. 3. Conductivity is found to increase by orders of magnitude with respect to undoped P(NDI2OD-T2) (4.6×10^{-7} $\pm$ 1.7×10^{-7} S cm^{-1}), thus indicating that all N-alkyl substituted 1H-benzimidazoles are effective dopants. Conductivity as a function of dopant concentration follows the general trend previously observed for the case of **DMBI** and is similar for all dopants: σ first increases with concentration, reaching a maximum in between 15% and 30% dopant concentration, and then decreases for higher concentrations. This decrease at high concentration was ascribed to phase segregation in the case of **DMBI**.[36] For films doped with dopants with linear alkyl chains, σ increases with increasing chain length. The maximum σ values are $1.8 \times 10^{-3} \pm 1.9 \times 10^{-4}$ S cm^{-1}, $3.4 \times 10^{-3} \pm 9.7 \times 10^{-4}$ S cm^{-1}, $4.0 \times 10^{-3} \pm 1.6 \times 10^{-4}$ S cm^{-1} and $4.1 \times 10^{-3} \pm 6.6 \times 10^{-4}$ S cm^{-1}, for **DMBI**, **DEtBI**, **DPrBI** and **DBuBI**, respectively. The maximum σ values for samples doped with the propyl and butyl derivatives are very close, thus suggesting that the effect of increasing the alkyl chain length is approaching a plateau. When doping P(NDI2OD-T2) with e N-alkyl-1H-benzimidazoles bearing branched chains, the highest conductivity value of $7.2 \times 10^{-3} \pm 1.4 \times 10^{-4}$ S cm^{-1} was achieved with **DiPrBI** at 25% doping, which is almost one order of magnitude higher than that obtained with **DMBI**. The **DiBuBI** showed a conductivity in the same range of the dopant with n-butyl substituents.

We also performed measurements to determine the Seebeck coefficients (α) of three representative polymer/dopant blends, namely the reference 1H-benzimidazole with methyl (**DMBI**), the dopant with linear chains giving the most effecting doping (**DBuBI**) and the dopant with branched chains giving the most effective doping (**DiPrBI**). The measured values of α at 363 K are always negative, as expected for a Seebeck effect dominated by
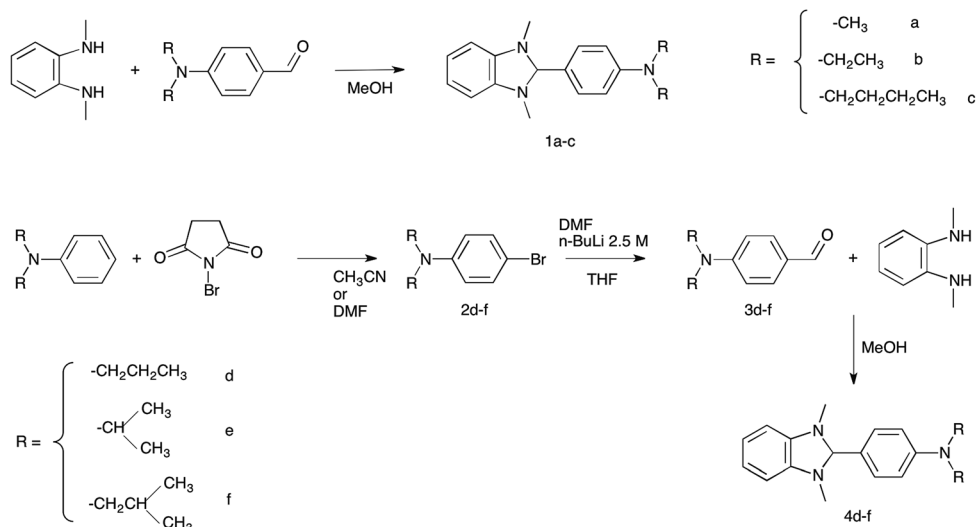
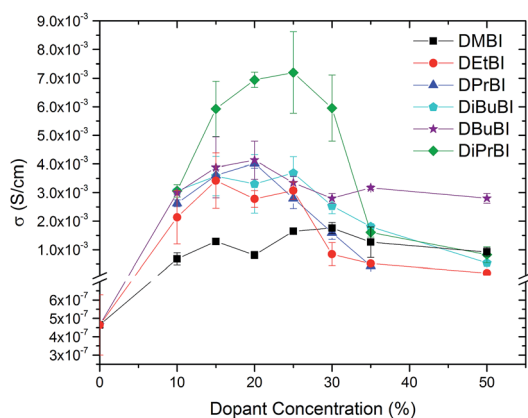Fig. 2 Synthetic routes for the realization of N-alkyl substituted 1H-benzimidazoles.

Fig. 3 Electrical conductivity σ vs. dopant concentration (from 10 to 50%) of all N-alkyl substituted 1H-benzimidazoles synthetized.

electrons, with values of −44 μV K^{-1} for the **DMBI**-doped sample, −35 μV K^{-1} for the **DBuBI**-doped sample and −32 μV K^{-1} for the **DiPrBI**-doped sample. These values are extracted with an error bar of ±15 μV K^{-1}, owing to the high sample electrical resistance. For the **DiPrBI**-doped sample which achieved the highest electrical conductivity, we also estimated the power factor (PF) at 363 K to be ∼1.1×10^{-3} μW mK^{-1}.

The temperature dependence of the electrical conductivity was measured for the same samples in order to characterize the activation energy (E_a) of σ (Fig. 4). In all cases, σ decreases with decreasing temperature, with the best fit achieved with a temperature dependence of $\ln \sigma(T) \propto T^{-1/2}$ (see ESI for details†), indicating a variable range hopping (VRH) transport regime with dimensionality of $d = 1$ as already reported previously.[37] Values for E_a of ∼330 meV were determined for each system. Therefore, the differences in σ cannot be ascribed to a modification of the transport properties, i.e. a difference in the energetic barriers experienced by charge carriers, but rather to the number of molecules effectively active in the doping

process. This evidence suggests that the different alkyl chains play a role in the polymer/dopant interaction and on the doping efficiency.

The microstructure of the different films was investigated first by acquiring the topography of the respective surfaces with AFM. Four types of exemplary samples were chosen: undoped P(NDI2OD-T2), P(NDI2OD-T2):**DMBI**, P(NDI2OD-T2):**DBuBI** and P(NDI2OD-T2):**DiPrBI**; in other words the blend with the lowest σ, the blend with the dopant with the longest linear alkyl chains and the blend with the highest σ, respectively. The undoped P(NDI2OD-T2) film surface shows a typical fiber-like morphology (Fig. 5). In all other cases, round features of varying number and size appear as well. In particular, the surface of P(NDI2OD-T2):**DiPrBI** film is similar to the undoped film, and it shows also a similar r.m.s. roughness ($R_{rms \ P(NDI2OD-T2)} = 0.76$ nm; $R_{rms \ P(NDI2OD-T2):DiPrBI} = 0.86$ nm). The doped sample with the lowest σ, instead, showed the highest surface roughness ($R_{rms \ P(NDI2OD-T2):DMBI} = 2.55$ nm), whereas the
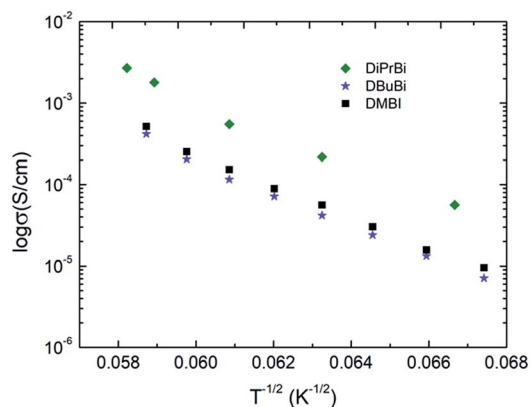

Fig. 4 Temperature dependence of electrical conductivity between 200 and 300 K for the polymer doped with three representative dopants at 20% concentration.
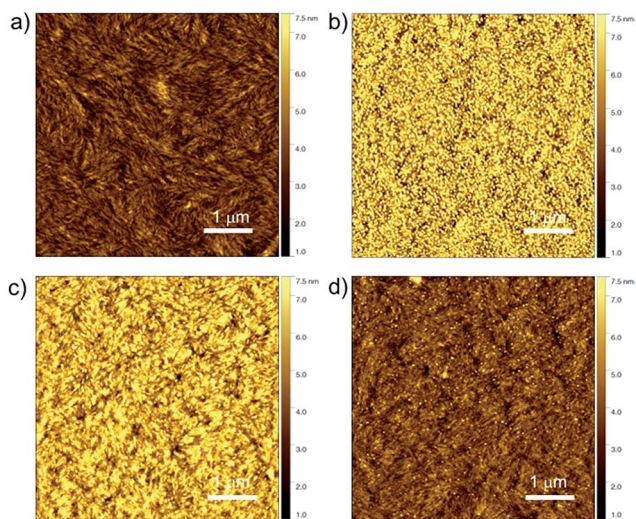
Fig. 5 Atomic force microscopy images of: (a) undoped P(NDI2OD-T2) film, (b) P(NDI2OD-T2) film doped with **DMBI**, (c) P(NDI2OD-T2) film doped with **DBuBI**, (d) P(NDI2OD-T2) film doped with **DiPrBI**. Dopant concentration is 20% for all samples.

sample with longest linear alkyl chains, characterized by an intermediate σ, has a roughness in between the above mentioned cases.

To obtain further insights into the aggregation/crystallization behaviour of P(NDI2OD-T2) in the presence of the various n-type dopants, synchrotron-based grazing-incidence wide-angle scattering (GIWAXS)[45] measurements were conducted. Two of the representative 2D GIWAXS patterns are displayed in Fig. 6a and b. As seen from Fig. 6a, the simultaneous appearance of in-plane (IP) ($h00$) and ($00l$) peaks, along with out-of-plane (OOP) (010) peak indicates that in undoped films P(NDI2OD-T2) crystallites adopt preferentially a face-on orientation with respect to the substrate.[46] Interestingly, well-defined OOP P(NDI2OD-T2) ($h00$)′ diffraction peaks occur with the incorporation of the dopants. Since these out-of-plane P(NDI2OD-T2) ($h00$)′ lamellar peaks are absent in the undoped P(NDI2OD-T2) thin films, incorporation of the dopant molecules induces an edge-on orientation of the crystallites. The 2D GIWAXS patterns of the remaining P(NDI2OD-T2):dopant films show a similar behaviour of varying extent (Fig. SI 11†). In addition, the absence of IP π–π stacking ($0k0$)′ with respect to OOP lamellar ($h00$)′ suggests that the dopant molecules may be disrupting the π–π stacking of the edge-on oriented P(NDI2OD-T2) chains. Diffraction peaks related to a dopant phase are absent, indicating either good intermixing of the dopant within the polymer matrix, or that the dopant molecules are unable to crystallize in the blend.

More quantitative structural information can be extracted from sector-averaged 1D GIWAXS profiles along OOP and IP, respectively.[47] The OOP profiles from Fig. 6c clearly show higher order ($h00$)′ diffraction peaks from all P(NDI2OD-T2):dopant blends, suggesting that all dopants, regardless of the nature of the alkyl side chain, are capable of inducing edge-on P(NDI2OD-T2) crystallites in the blends. Intriguingly, the

incorporation of dopant molecules has a distinct effect on P(NDI2OD-T2) crystallites along different crystallographic axis. As shown in Fig. 6d, the IP P(NDI2OD-T2) ($h00$) lamellar stacking peaks of residual face-on crystallites in the blends shift toward higher values of q (magnitude of the scattering vector) after the blending with dopants, while the P(NDI2OD-T2) ($00l$) backbone stacking peaks retain a constant q value. This observation implies that the dopants reduce the lamellar spacing of P(NDI2OD-T2) the face-on crystallites, without disrupting the originally well-ordered backbone arrangement. Although IP lamellar stacking direction does not contribute to charge transport, the obvious changes of lamellar spacing with the addition of dopants unambiguously point out that strong molecular interaction between P(NDI2OD-T2) and dopants exists. Further details can be obtained from the 1D GIWAXS profiles around the OOP (200)′ peaks and IP (004) peaks, which are chosen for closer investigation since they do not show overlap with other diffraction peaks. As plotted in Fig. 6e, different dopants induce different populations of edge-on P(NDI2OD-T2) crystallites, evidenced by the varying OOP (200)′ diffraction intensity in thin films with similar film thickness. The dopant-induced edge-on P(NDI2OD-T2) crystallites may be one of the contributors for the enhanced σ compared to the undoped P(NDI2OD-T2) thin film. However, the fact that the best performing P(NDI2OD-T2):**DiPrBI** thin film only exhibits an intermediate level of edge-on crystallinity as indicated by the plots around OOP (200)′ region, implies that other factors are contributing to the improvement of σ. In addition, the impact of the dopants on the P(NDI2OD-T2) backbone stacking has been investigated by examining the IP P(NDI2OD-T2) (004) peaks as shown in Fig. 6f. It is apparent that the incorporation of all dopants, except for **DMBI**, slightly reduces the crystallinity of P(NDI2OD-T2) backbone stacking, evidenced by the moderate reduction of the IP P(NDI2OD-T2) (004) peak intensity. The **DMBI**, on the other hand, almost eliminates the IP P(NDI2OD-T2) (004) peak, suggesting that the **DMBI** dopant molecules tend to disrupt the ordered arrangement of P(NDI2OD-T2) molecules along the backbone direction. This observation matches well with the AFM images where the largest surface roughness and the lowest σ is observed for P(NDI2OD-T2):**DMBI**. Lastly, the crystallite orientation distribution (COD) profiles of the dopant-induced edge-on P(NDI2OD-T2) crystallites have also been examined. Although no linear correlation between COD and conductivity was found (see Fig. SI 12†), the different COD extracted from the P(NDI2OD-T2) thin films with various dopants provides direct evidence that different molecular structures of dopants impact the preferential orientation of P(NDI2OD-T2) crystallites distinctly. Notably the P(NDI2OD-T2):**DMBI** has the broadest COD supporting the higher degree of disorder in this blend which may contribute to its low σ.

We interpret these observations by intercalation of dopants in between P(NDI2OD-T2) backbones. Such a picture is in agreement with the higher q values of the ($h00$)′ reflections in the blend. Due to intercalation, the average distance between two P(NDI2OD-T2) backbones increases generating additional space for the amorphous alkyl chain layers, which finally leads
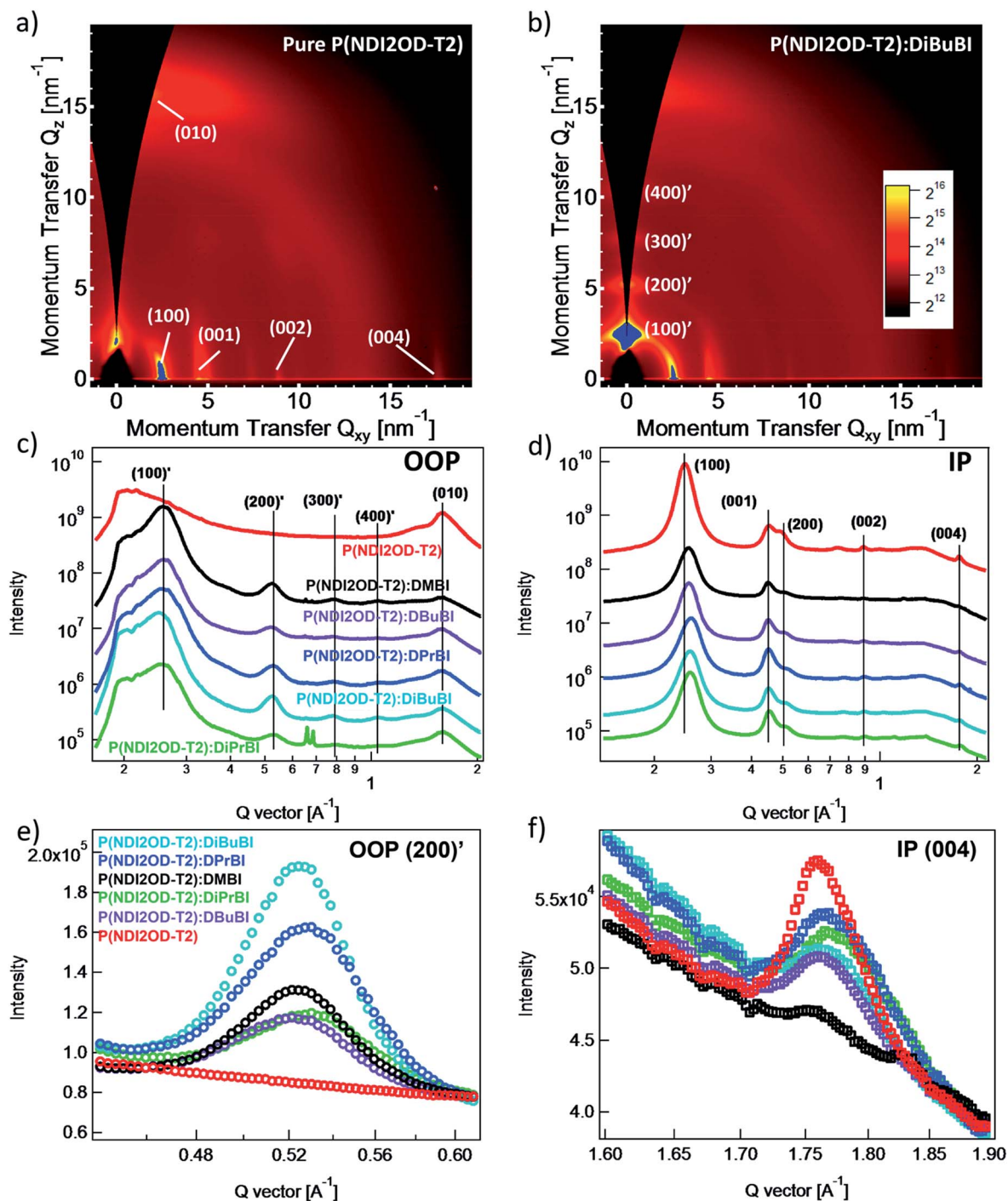
Fig. 6 2D grazing-incidence wide-angle X-ray scattering (GIWAXS) patterns for (a) pure P(NDI2OD-T2) and (b) P(NDI2OD-T2): DiBuBI, plotted with identical intensity scale. The sector-averaged 1D profiles along out-of-plane (OOP) and in-plane are plotted in (c) and (d), respectively. Note the sharp peaks around 0.6 Å^{-1} < q < 0.7 Å^{-1} in P(NDI2OD-T2):DiPrBI along OOP is parasitic scattering from upstream beamline. The close-up profiles for dopant induced P(NDI2OD-T2) (200)' diffraction along OOP and P(NDI2OD-T2) (004) along IP are also demonstrated in (e) and (f), respectively.

to contraction in (h00)' direction. Also, the less prevalent π–π stacking peak can be rationalized by dopant intercalation.

These results are finally corroborated by differential scanning calorimetry measurements on blends, where a new endotherm is observed at 30–40 K higher than $T_{m,dopant}$, that neither arises from the pristine dopant nor from P(NDI2OD-T2) (Fig. SI 8†). Although a reliable quantification of the corresponding melting enthalpy ΔH_m is not possible, on a qualitative basis ΔH_m increases with increasing doping concentration (Fig. S9†).

A chemical reaction of the dopant and the copolymer matrix as an alternative origin for the new endotherm can be excluded as samples were fully soluble after the DSC measurements and

the corresponding NMR spectra did not show other signals than those of dopant and copolymer (data not shown).

The observation of intercalation of **DMBI** and its derivatives is different compared to the findings of Schlitz *et al.*[36] and also to the miscibility behaviour of P(NDI2OD-T2) and DPBI, which is the phenyl-derivative of **DMBI**. Shin *et al.* reported segregation and crystallization of DPBI in P(NDI2OD-T2):DPBI blends processed from chlorobenzene, leading to dopant melting in as-prepared blends.[38] While the different structure of DPBI compared to **DMBI** may be one of the reasons for the different behaviour, it is also possible that the solvent has a prominent effect. Dichlorobenzene, as used here, is a better solvent for P(NDI2OD-T2) compared to chlorobenzene, which was used by Neher *et al.*[48] Thus, the presence of a larger amount of P(NDI2OD-T2) aggregates may promote the segregation of dopant already in chlorobenzene solution, while dopant intercalation may be favoured for processing from dichlorobenzene where less aggregated, *i.e.* more molecularly dissolved chains, are present. Hence, solvent quality may be important for controlling intercalation, which will be the subject of further investigations.

Conclusions

We have designed, synthesized and characterized a series of new air-stable 1*H*-benzimidazole-based dopants to study the effect of the dopant alkyl substituents on morphology and electrical properties of blends with the copolymer P(NDI2OD-T2). It was demonstrated that dopants with increasingly longer linear alkyl chains give rise to higher σ values. Up to four times higher conductivities (4.1×10^{-3} S cm^{-1}) were obtained for *n*-butyl-substituted dopants compared to the reference having methyl groups (**DMBI**). Dopants with branched alkyl chains were also studied. The highest σ was obtained from blends with isopropyl-substituted dopants (7×10^{-3} S cm^{-1}). Conductivity measurements as function of the temperature highlighted that charge transport follows a thermally activated, monodimensional variable range hopping (VRH) regime. Moreover, the activation energies were found to be very similar for all the doped samples irrespective of dopant, specifically ~330 meV, indicating similar energetic barriers for transport. Structural analysis showed that the dopant molecules induce an edge-on orientation of polymer crystallites, a decrease in the lamellar stacking distance, and a disruption of backbone and π-stacking order compared to pristine P(NDI2OD-T2) films. These observations, along with presence of a new endotherm in the blend, provide evidence for the intercalation of the dopant molecules between P(NDI2OD-T2) chains.

Overall, our work demonstrates that, besides tailoring of the conjugated backbone, the engineering of the solubilizing chains in small molecular dopants is an effective strategy to control and improve the miscibility of dopants and polymers. This strategy allows to maintain the electron transfer process, while optimizing the conductivity thanks to an improved doping efficiency. Such a result, which is particularly relevant for n-type doping, is important for the development of advanced opto-electronic organic devices and efficient organic thermo-electric generators.

Conflicts of interest

There are no conflicts to declare.

Acknowledgements

References

1 S. Kola, J. Sinha and H. E. Katz, *J. Polym. Sci., Part B: Polym. Phys.*, 2012, **50**, 1090–1120.
2 D. Natali and M. Caironi, *Adv. Mater.*, 2012, **24**, 1357–1387.
3 P. Lin and F. Yan, *Adv. Mater.*, 2012, **24**, 34–51.
4 X. Guo, M. Baumgarten and K. Müllen, *Prog. Polym. Sci.*, 2013, **38**, 1832–1908.
5 I. Etxebarria, J. Ajuria and R. Pacios, *Org. Electron.*, 2015, **19**, 34–60.
6 N. Thejo Kalyania and S. J. Dhoble, *Renewable Sustainable Energy Rev.*, 2012, **16**, 2696–2723.
7 K. Walzer, B. Männig, M. Pfeiffer and K. Leo, *Chem. Rev.*, 2007, **107**, 1233–1271.
8 M. Chang, G. Lim, B. Park and E. Reichmanis, *Polymers*, 2017, **9**, 212.
9 R. Noriega, J. Rivnay, K. Vandewal, F. P. V. Koch, N. Stingelin, P. Smith, M. F. Toney and A. Salleo, *Nat. Mater.*, 2013, **12**, 1038–1044.
10 L.-L. Chua, J. Zaumseil, J.-F. Chang, E. C.-W. Ou, P. K.-H. Ho, H. Sirringhaus and R. H. Friend, *Nature*, 2005, **434**, 194–199.
11 D. Fazzi and M. Caironi, *Phys. Chem. Chem. Phys.*, 2015, **17**, 8573–8590.
12 Y. Chen, Y. Zhao and Z. Liang, *Energy Environ. Sci.*, 2015, **8**, 401–422.
13 O. Bubnova and X. Crispin, *Energy Environ. Sci.*, 2012, **5**, 9345.
14 M. V. Fabretto, D. R. Evans, M. Mueller, K. Zuber, P. Hojati-Talemi, R. D. Short, G. G. Wallace and P. J. Murphy, *Chem. Mater.*, 2012, **24**, 3998–4003.
15 N. Kim, S. Kee, S. H. Lee, B. H. Lee, Y. H. Kahng, Y. R. Jo, B. J. Kim and K. Lee, *Adv. Mater.*, 2014, **26**, 2268–2272.
16 O. Bubnova, Z. U. Khan, H. Wang, S. Braun, D. R. Evans, M. Fabretto, P. Hojati-Talemi, D. Dagnelund, J.-B. Arlin, Y. H. Geerts, S. Desbief, D. W. Breiby, J. W. Andreasen, R. Lazzaroni, W. M. Chen, I. Zozoulenko, M. Fahlman, P. J. Murphy, M. Berggren and X. Crispin, *Nat. Mater.*, 2013, **13**, 190–194.
17 D. M. de Leeuw, M. M. J. Simenon, A. R. Brown and R. E. F. Einerhand, *Synth. Met.*, 1997, **87**, 53–59.

18 B. A. Jones, A. Facchetti, M. R. Wasielewski and T. J. Marks, *J. Am. Chem. Soc.*, 2007, **129**, 15259–15278.

19 C. K. Chiang, S. C. Gau, C. R. Fincher Jr, Y. W. Park, A. G. MacDiarmid and A. J. Heeger, *Appl. Phys. Lett.*, 1978, **33**, 18.

20 D. M. Ivory, G. G. Miller, J. M. Sowa, L. W. Shacklette, R. R. Chance and R. H. Baughman, *J. Chem. Phys.*, 1979, **71**, 1506–1507.

21 A. Ali Benamara, M. Galtier and A. Montaner, *Synth. Met.*, 1991, **41**, 45–48.

22 G. Parthasarathy, C. Shen, A. Kahn and S. R. Forrest, *J. Appl. Phys.*, 2001, **89**, 4986.

23 C.-C. Chang, M.-T. Hsieh, J.-F. Chen, S.-W. Hwang and C. H. Chen, *Appl. Phys. Lett.*, 2006, **89**, 253504.

24 P.-C. Kao, J.-Y. Wang, J.-H. Lin and C.-H. Yang, *Thin Solid Films*, 2013, **527**, 338–343.

25 P.-C. Kao, J.-H. Lin, J.-Y. Wang, C.-H. Yang and S.-H. Chen, *J. Appl. Phys.*, 2011, **109**, 094505.

26 A. Barbot, B. Lucas, C. Di Bin and B. Ratier, *Org. Electron.*, 2014, **15**, 858–863.

27 P.-C. Kao, C.-C. Chang and S.-Y. Lin, *Surf. Coat. Technol.*, 2013, **231**, 135–139.

28 D.-Y. Zhou, F.-S. Zu, Y.-J. Zhang, X.-B. Shi, H. Aziz and L.-S. Liao, *Appl. Phys. Lett.*, 2014, **105**, 83301.

29 P. M. Grant, R. L. Greene, G. C. Wrighton and G. Castro, *Phys. Rev. Lett.*, 1973, **31**, 1311.

30 K. P. Goetz, D. Vermeulen, M. E. Payne, C. Kloc, L. E. McNeil and O. D. Jurchescu, *J. Mater. Chem. C*, 2014, **2**, 3065–3076.

31 A. Nollau, M. Pfeiffer, T. Fritz and K. Leo, *J. Appl. Phys.*, 2000, **87**, 4340–4343.

32 T. Menke, P. Wei, D. Ray, H. Kleemann, B. D. Naab, Z. Bao, K. Leo and M. Riede, *Org. Electron.*, 2012, **13**, 3319–3325.

33 P. Wei, T. Menke, B. D. Naab, K. Leo, M. Riede and Z. Bao, *J. Am. Chem. Soc.*, 2012, **134**, 3999–4002.

34 X.-Q. Zhu, M.-T. Zhang, A. Yu, C.-H. Wang and J.-P. Cheng, *J. Am. Chem. Soc.*, 2008, **130**, 2501–2516.

35 P. Wei, J. H. Oh, G. Dong and Z. Bao, *J. Am. Chem. Soc.*, 2010, **132**, 8852–8853.

36 R. Schlitz, F. G. Brunetti, A. M. Glaudell, P. L. Miller, M. A. Brady, C. J. Takacs, C. J. Hawker and M. L. Chabinyc, *Adv. Mater.*, 2014, **26**, 2825–2830.

37 S. Wang, H. Sun, U. Ail, M. Vagin, P. O. Å. Persson, J. W. Andreasen, W. Thiel, M. Berggren, X. Crispin, D. Fazzi and S. Fabiano, *Adv. Mater.*, 2016, **28**, 10764–10771.

38 Y. Shin, M. Massetti, H. Komber, T. Biskup, D. Nava, G. Lanzani, M. Caironi and M. Sommer, *Adv. Electron. Mater.*, 2018, **1700581**, 1700581.

39 Y. Wang, M. Nakano, T. Michinobu, Y. Kiyota, T. Mori and K. Takimiya, *Macromolecules*, 2017, **50**, 857–864.

40 J. Liu, L. Qiu, G. Portale, M. Koopmans, G. ten Brink, J. C. Hummelen and L. J. A. Koster, *Adv. Mater.*, 2017, 1701641.

41 B. D. Naab, S. Guo, S. Olthof, E. G. B. Evans, P. Wei, G. L. Millhauser, A. Kahn, S. Barlow, S. R. Marder and Z. Bao, *J. Am. Chem. Soc.*, 2013, **135**, 15018–15025.

42 D. Beretta, P. Bruno, G. Lanzani and M. Caironi, *Rev. Sci. Instrum.*, 2015, **86**, 75104.

43 N. M. Kirby, S. T. Mudie, A. M. Hawley, D. J. Cookson, H. D. T. Mertens, N. Cowieson and V. Samardzic-Boban, *J. Appl. Crystallogr.*, 2013, **46**, 1670–1680.

44 J. Ilavsky, *J. Appl. Crystallogr.*, 2012, **45**, 324–328.

45 C. J. Schaffer, C. Wang, A. Hexemer and P. Müller-Buschbaum, *Polymer*, 2016, **105**, 1–11.

46 J. Rivnay, R. Steyrleuthner, L. H. Jimison, A. Casadei, Z. Chen, M. F. Toney, A. Facchetti, D. Neher and A. Salleo, *Macromolecules*, 2011, **44**, 5246–5255.

47 J. Min, X. Jiao, I. Ata, A. Osvet, T. Ameri, P. Bäuerle, H. Ade and C. J. Brabec, *Adv. Energy Mater.*, 2016, **6**, 1–9.

48 R. Steyrleuthner, M. Schubert, I. Howard, B. Klaumünzer, K. Schilling, Z. Chen, P. Saalfrank, F. Laquai, A. Facchetti and D. Neher, *J. Am. Chem. Soc.*, 2012, **134**, 18303–18317.